## Subproject F1.3

# Nanoscale Transparent Conductive Oxides

**Principle Investigators: Claus Feldmann**

**CFN-Financed Scientists: Elin Hammarberg (1/2 E13, 12 months), Silke Wolf (1/2 E13, 6 months), Hailong Dong (1/2 E13, 18 months)**

**Further Scientists: Jan Ungelenk**

**Institut für Anorganische Chemie**
**Karlsruhe Institute of Technology (KIT)**

**F1.3** Feldmann

# Nanoscale Transparent Conductive Oxides

## Introduction and Summary

Transparent Conductive Oxides (TCOs) are of major technical importance regarding transparent electrodes (e.g., in displays, solar cells, organic light emitting diodes - OLEDs) as well as for IR-reflection (e.g., energy saving windows). Nowadays, indium tin oxide (ITO, $In_2O_3$:Sn), which is typically applied as a thin layer on glass substrates, represents the state-of-the-art. Relevant ITO layers are conventionally prepared via gas-phase deposition, for instance, magnetron sputtering, chemical vapor deposition, vacuum evaporation or spray pyrolysis. At the optimum, resistivities in the order of $10^{-4}$ Ω cm, sheet resistivities of about 10 Ω/□ and a transparency of 85-90 % have been realized based on ITO.

With this CFN-subproject a microwave heating is applied to prepare suspensions of $In_2O_3$:Sn (ITO), ZnO:In (IZO) and ZnO:Al (AZO) nanocrystals in diethylene glycol as a high-boiling multidentate alcohol (so-called polyol). All these n-doped oxides are realized with high yields and in suspensions with solid contents up to 10 wt-%. The suspensions are colloidally stable for months. According to dynamic light scattering, scanning electron microscopy, transmission electron microscopy, X-ray diffraction patterns and Brunauer-Emmett-Teller analysis as-prepared particles turn out to be single crystalline with an average diameter of 8−15 nm, a near monodisperse size distribution, and a low degree of agglomeration. As-prepared samples exhibit high resistivities due to the adhesion of DEG as a stabilizer on the particle surface. Subsequent to a specific thermal post-treatment resistivities of 1.1 x $10^{-2}$ Ω cm, $2.0 \cdot 10^{-1}$ Ωcm and $5.7 \cdot 10^{-1}$ Ωcm are obtained for ITO, IZO and AZO powders, respectively. As a proof of the concept, thin layers are deposited on glass plates using a simple solvent evaporation technique. Post-treated layers exhibit a visible transmittance of about 80 % and resistivities of 1.2 x $10^{-2}$ Ω cm (ITO), $2.1 \cdot 10^{-1}$ Ωcm (IZO) and $2.6 \cdot 10^{-1}$ Ωcm (AZO).

While searching for novel TCO materials, the unique phase composition β-$Sn_{1-n}WO_4$ · n α-Sn, including nanoscale incipient crystalline β-$SnWO_4$ and α-Sn was gained and turned out to be a very promising photocatalyst under simulated daylight. Since the nanomaterial is gained via a quick and simple precipitation in water, the synthesis can be regarded as “real green”. Despite the simple preparation, the nanoparticles are of high quality, exhibiting an average diameter of 20 nm, a low degree of agglomeration, a high specific surface and an efficient electrostatic stabilization. As-prepared β-$Sn_{1-n}WO_4$ · n α-Sn exhibits a strong absorption in the visible spectral range (554 nm, 2.2 eV) and a lasting high photocatalytic performance under simulated daylight. Various organic dyes (phenothiazine dye methylene blue, triphenylmethane dye basic green 4, azo-dye methyl red) are decomposed with significantly higher degradation rates (5−10) as compared to commercially available Degussa P25 ($TiO_2$, anatase). Recycling experiments prove the phase stability and reusability of as-prepared β-$Sn_{1-n}WO_4$ · n α-Sn.

Transparent conductive oxides as prepared in this CFN-subproject were transferred to several cooperation partners, including organic thin-film solar cells (CFN member U. Lemmer, CFN member H. Kalt, Konarka company), Cu(Ga,In)$Se_2$-based thin-film solar cells (Dr. E. Ahlswede, Zentrum für Solarenergie und Wasserstoffforschung, Stuttgart), printed thin-film electronics (CFN member H. Hahn), sensor applications (Priv.-Doz. U. Weimar, Universität Tübingen), characterization via solid state NMR (Dr. J. Schmedt a.d.G., LMU München).

In the timeframe 2008-2010, subproject F1.3 has led to 8 publications, among which is 1 review in *Angew. Chem.*, 1 in *Chem. Mater.*, 1 in *Applied Catal. B* and 1 in *Chem. Mater.*.

## 1. Indium tin oxide (ITO)

According to this study nanocrystalline $In_2O_3$:Sn is realized via a polyol-mediated synthesis. To this concern, solutions of first, $InCl_3 \cdot 4\ H_2O$ and $SnCl_4 \cdot 5\ H_2O$ and second, $N(CH_3)_4OH \cdot 5\ H_2O$, both in DEG were mixed. Mixing was followed by immediate formation of particles. The underlying nucleation process turned out to be optimal at slightly elevated temperatures (80 °C). Thereafter the resulting suspension was heated for 2 h at 200 °C in order to boost materials crystallinity. Due to the boiling point of DEG (248 °C)[1], heating was performed at ambient pressure. DEG furthermore stabilizes the particle surfaces during nucleation and crystallization, and therefore prevents particle growth and aggregation. This stabilizing effect of multidentate and high-boiling alcohols (so-called polyols, e.g. diethylene glycol/DEG, ethylene glycol/EG, glycerine/GLY) has been already described and used to prepare a wide range of nanoscale materials, including elemental metals, oxides, sulfides or fluorides.[2-6] Again, the efficient stabilization of nanoscale materials by a polyol is confirmed here. The application of microwave irradiation turned out to be very advantageous with regard to particle morphology and material crystallinity. A comparable situation has been described for other compounds, such as nanoscale Ag, Au, Pt, CdSe or $Bi_2S_3$.[7-11]

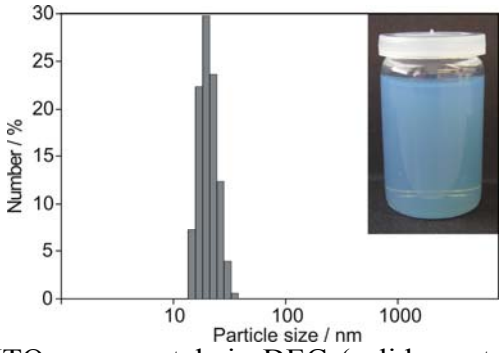


**Figure 1.** As-prepared ITO nanocrystals in DEG (solids content: 0.62 wt.-%) and size distribution thereof.

As-prepared suspensions of ITO in DEG are colloidally stable within weeks and exhibit a transparent appearance with a bright blue color (figure 1). Qualitatively this finding already hints to the presence of sufficiently doped $In_2O_3$:Sn nanocrystals. Size and size distribution of as-prepared ITO particles were quantified by dynamic light scattering (figure 1). To this concern, the average particle diameter is evidenced to a value of 19(1) nm with an almost monodispersed size distribution. Subsequent to centrifugation and drying, as-prepared $In_2O_3$:Sn can be separated from the suspension and was yielded as a blue powder in quantities of 92 %. Scanning electron microscopy reveals the as-prepared particles to be non-agglomerated, and with spherical and very uniform morphology (figure 2). SEM images were also used for a statistical evaluation of particle diameter and size distribution. To this end, the mean diameter was deduced based on 320 particles and amounts to 15(1) nm. This value is in very good agreement with DLS analysis, considering an enlarged hydrodynamic diameter in the latter case. Finally, nitrogen absorption measurements of powder samples were performed according to the Brunauer-Emmett-Teller (BET) type of method. Herein a specific surface of 56.1 $m^2\ g^{-1}$ was measured. Assuming spherical and non-porous ITO particles with a density of bulk $In_2O_3$, this value corresponds to a particle diameter of 15 nm, which is again in accordance with SEM and DLS analysis.

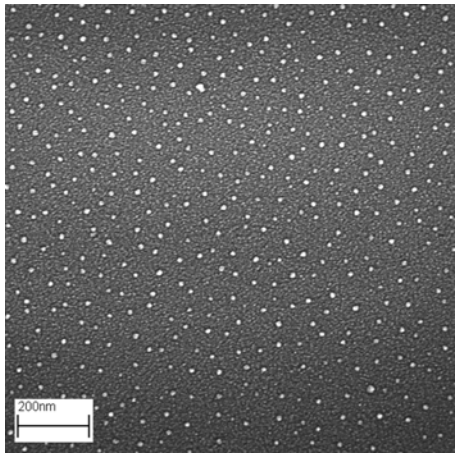


**Figure 2.** SEM image of as-prepared ITO nanocrystals.

The crystallinity of as-prepared ITO is evidenced based on X-ray powder diffraction analysis (XRD) as well as with high-resolution transmission electron microscopy (HRTEM). First, XRD evidences powder samples to crystallize with a $CaF_2$-defect type superstructure. Even more important, the hexagonal $In_2O_3$ phase, which is expected - according to the step rule by Ostwald - for a liquid-phase approach and which is known for its significantly lower conductivity, turned out to be completely absent. Via the Scherrer equation, powder diffraction patterns can also be used to calculate the crystallite size. From the three most intensive Bragg peaks - (222), (400), and (440) - an average crystallite size of 18 nm was obtained. Taking the particle diameter stemming from DLS and SEM analysis into account, this confirms the single crystallinity of the as-prepared ITO particles. This view is further confirmed by HRTEM. Representative images display ITO nanoparticles with highly ordered lattice fringes, indicating that even areas close to the particle surface are well crystallized (figure 3). Two lattice plane distances were identified from HRTEM images: 2.93 and 2.54 Å. This again proves the presence of cubic $In_2O_3$ (lattice plane (222) with 2.92 Å and (400) with 2.53 Å). In summary, size, size distribution, and crystallinity of as-prepared ITO particles were investigated based on several independent analytical tools and result in a very good agreement. Moreover, microwave-assisted heating turned out to be essential. If a conventional resistance heating (e.g. heating mantle) is performed at similar temperature and time of heating ITO remained amorphous.

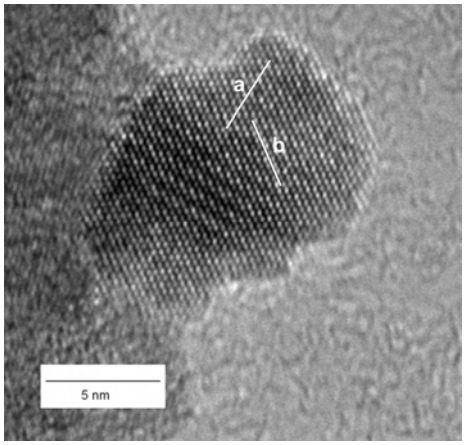


**Figure 3.** HRTEM image of as-prepared ITO nanocrystal with lattice plane distances denoted, where *a* corresponds to 10 lattice planes with a distance of 2.93 Å and *b* to 10 lattice planes with a distance of 2.54 Å.

Former investigations addressing a polyol-mediated synthesis have shown that the polyol as a coordinating, and thereby stabilizing agent is adhered on the particle surface. Even washed and dried powder materials contain the multidentate alcohol in quantities of a monolayer.[13,14] Since this monolayer might hinder the interparticular electron transfer, prior to electrical conductivity the surface conditioning is investigated. To this concern, FT-IR spectra of as-prepared ITO powder were recorded. As expected, the transmittance of ITO is very low in the wavenumber interval of 7000-2000 $cm^{-1}$. Since a high IR reflectivity implies a large number of free carriers, the conductivity of as-prepared ITO particles should be high, too. Vibration bands are visible at 1084, 610, and 500 $cm^{-1}$. Hereof, the two at lower wavenumber can be ascribed to phonon absorptions of the $In_2O_3$ lattice.[15] The absorption at 1084 $cm^{-1}$ is attributed to the valence vibration ν(C-O) of DEG adhered on the particle surface. To quantify the amount of DEG, thermal analysis (DTA/TG) was carried out. Here, a weight loss of 0.3 % is observed between 200 and 400 °C, which can be related to DEG.[13,14] Taking both - the specific surface and the low weight loss of as-prepared ITO - into account, a significant influence on the conductivity of powder samples is not to be expected. In order to reduce the influence of the grain boundaries and to initiate a close interparticulate contact, the nanocrystalline ITO powder was pressed to form dense pellets. Via four-point probing, a sheet resistivity of 4.0 Ω/ was measured. Considering a pellet thickness of 26 µm, this corresponds to a specific resistivity of 1.1 x $10^{-2}$ Ω cm. Thus, it can be concluded that as-prepared $In_2O_3$:Sn (5 mol-%) powder shows a considerable conductivity. This is even more surprising since in contrast to literature neither a thermal nor a chemical post-treatment is required (e.g., to remove all hydroxyl contents, to burn out organic residues, to reduce lattice defects, or to establish a sufficient carrier concentration).

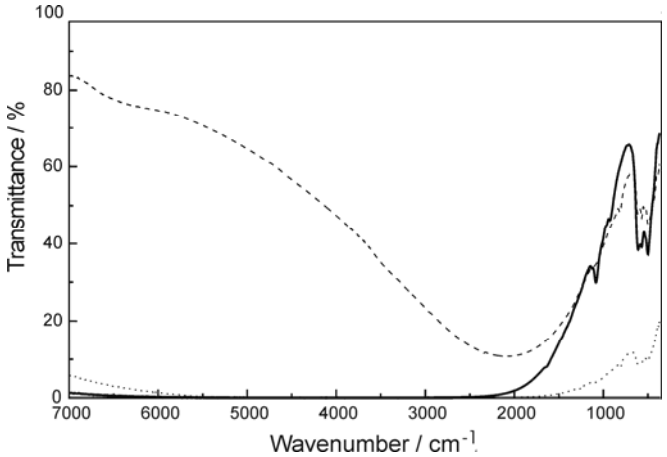


**Figure 4.** FT-IR sprectra of ITO powder samples: as-prepared (solid), after thermal treatment in air at 500 °C (dashed), and after reduction with forming gas at 300 °C (dotted).

Aiming at thin films on transparent substrates, as a proof of concept $In_2O_3$:Sn (5 mol-%) nanocrystals suspended in DEG and 1-methoxy-2-propanol were spread and dried on glass plates. The suspensions were applied here without any further optimization of, for instance, viscosity, solids content, type of solvent, or substrate pre-conditioning. In contrast to pressed pellets, the resulting films only showed a minor conductivity. This finding is attributed to their incompactness. In order to increase the particle-to-particle contact, as-deposited films were firstly treated thermally in air (500 °C, 1 h), and secondly treated with forming gas ($N_2$:$H_2$ = 90:10, 300 °C, 2 h). For comparison, this treatment was also conducted with powder samples. According to FT-IR spectra, first the transmittance of ITO is considerably increased above 2000 $cm^{-1}$ (figure 4). This is due to a filling of lattice defects with oxygen and in correspondence with a significantly reduced number of free carriers. To repopulate the level of free carriers, ITO was reduced with forming gas as a second

step. With this measure, the IR-transmittance was reestablished and partly even further decreased. Consequently, the relevant lattice defects were recreated, and the free carrier concentration should thus be re-increased, too. In the case of ITO coated glass plates, the described post-treatment resulted in a sheet resistance of 295 Ω/ . The film thickness was estimated to 400 nm from SEM images. As a consequence, a specific resistivity of 1.2 x $10^{-2}$ Ω cm is gained without applying any correction factor for porosity. Since a considerable porosity can be assumed, the resistivity of the particles themselves will be even lower. The high conductivity of post-treated films indicates that the low conductivity of as-prepared layers is indeed due to insufficient particle-to-particle contacts. Finally, UV-VIS spectra of post-treated, ITO-coated glass plates show a transmittance similar to uncoated the glass plate. This indicates an excellent transmittance in the visible (figure 5). Based on this proof of concept significantly improved layers (e.g. with concern to homogeneity and density), and thereby increased conductivities are to be expected while applying professional printing technologies.

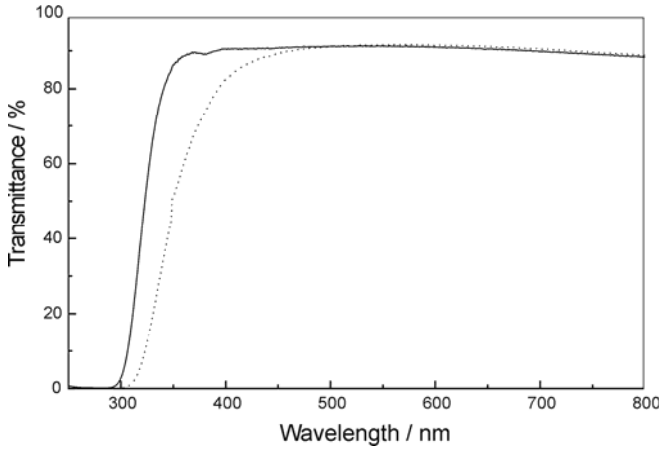


**Figure 5.** UV-VIS spectra of ITO-coated (dotted) and uncoated glass plate (solid).

## 2. Doped zinc oxides (AZO, IZO)

According to this study, nanocrystalline doped and non-doped ZnO is realized via a polyol-mediated synthesis. To this concern, solutions of $Zn(CH_3COO)_2 \cdot 2\,H_2O$ and $InCl_3 \cdot 4\,H_2O$ or $AlCl_3 \cdot 6\,H_2O$ in DEG were heated via microwave irradiation at 200 °C for 30 min. In accordance with the boiling point of DEG (248 °C), heating was performed at ambient pressure. DEG furthermore stabilizes the particle surfaces during nucleation and crystallization, and therefore prevents particle growth and aggregation. The stabilizing effect of these so-called polyols - namely a multidentate and high-boiling alcohol (e.g., diethylene glycol/DEG, ethylene glycol, glycerol) - is well known and has been already used to prepare a wide range of nanoscale materials, including elemental metals, oxides, sulfides and fluorides.[16–19] The efficient polyol-mediated stabilization of nanoparticles is again confirmed here. Heating by means of microwave-irradiation turned out to be very advantageous with regard to particle morphology and materials crystallinity as well. Thus, microwave-accelerated irradiation led to a much faster heating rate than conventional heating, and thereby resulted in a more precise control of nucleation and growth. We have earlier utilized this procedure and effect when preparing ITO nanocrystals. A comparable situation has been also reported by other authors for a polyol-mediated synthesis[20,21] as well as for a microwave-accelerated synthesis of nanoscale compounds, in general.[22–26] Since the hydrolysis of $Zn(ac)_2$ yielded non-crystalline intermediate $Zn(OH)_2$ at first, dehydration and crystallization of ZnO was promoted by increasing the temperature up to 200 °C as well as by distilling of all volatiles (e.g., excess water).

As-prepared suspensions of IZO (5.0 mol-% In) and AZO (5.0 mol-% Al) in DEG with different solid contents are colloidally stable within months. AZO suspensions exhibit a slight bluish shade, whereas IZO suspensions are bright blue. Qualitatively, this finding already hints to the incorporation of the dopants in the ZnO lattice. Subsequent to centrifugation and drying, as-prepared IZO and AZO powders could be separated from the suspension and were yielded in quantities of about 90 % for all samples. In the following, characterization and properties are presented for four samples with a low as well as high with a solid contents: IZO-1 (0.7 wt-%), IZO-2 (8.7 wt-%), AZO-1 (0.7 wt-%), and AZO-2 (9.2 wt-%). In order to determine the particle size distribution in the liquid phase, dynamic light scattering (DLS) was involved. First, all suspensions were diluted with DEG (about a factor of 1:100) subsequent to DLS measurement in order to exclude concentration artifacts. Figure 6 shows the results for IZO-1 and AZO-1. The resulting average hydrodynamic diameters are 15(1) nm and 12(1) nm for IZO and AZO, respectively. Hence, IZO and AZO particles are of similar size and have an almost monodisperse particle size distribution. DLS measurements of IZO-2 and AZO-2 after dilution resulted in an average hydrodynamic diameter of 16(1) nm and 13(1) nm, respectively. Thus, the particle size is only weakly affected by the solid contents of the suspension. In addition to diluted suspensions DLS measurements were secondly conducted after redispersion with high solid contents of 10 wt-%. The resulting average hydrodynamic diameters range from 29(2) nm (IZO-1) to 79(3) nm (AZO-2). These values can be interpreted as the mean agglomerate size at this particular concentration. Obviously, free Brownian motion of individual particles is hampered in concentrated suspensions. However, this finding is not related to a formation of hard aggregates since the hydrodynamic diameter again drops to the value of primary particles after dilution. Note also that even concentrated suspensions are colloidally stable and with hydrodynamic diameters clearly below 100 nm.

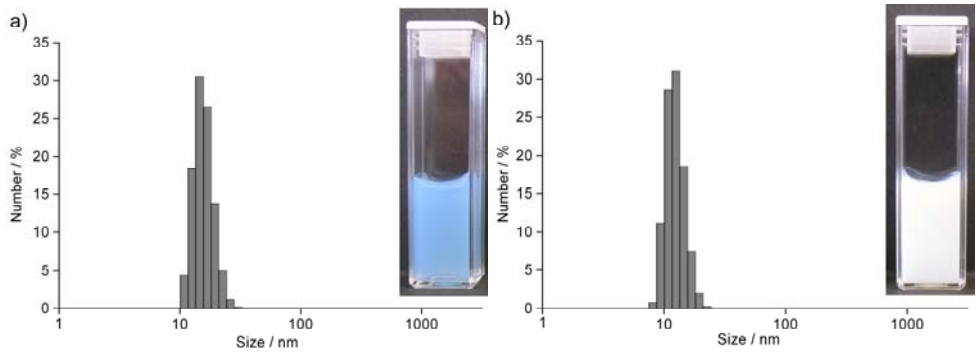


**Figure 6.** DLS measurements of a) IZO-1 and b) AZO-1 in DEG.

SEM investigations of diluted suspensions in DEG revealed as-prepared particles for all samples to be non-agglomerated, and with spherical and very uniform morphology (Fig. 7). SEM images were also used for statistical evaluation of the particle diameter. Calculations are based on more than 400 particles per sample. Finally, nitrogen absorption measurements were performed according to the BET type of method aiming at the size and degree of agglomeration of dried powder samples. Here, specific surfaces of 110 and 82 $m^2g^{-1}$ were measured for IZO-1 and AZO-1, respectively. Assuming the presence of spherical and non-porous particles with a density of bulk ZnO, these values correspond to particle diameters of 10 nm (IZO) and 22 nm (AZO). BET measurements of IZO-2 and AZO-2 show similar results. Taking the accuracy of the diameter stemming from BET analysis into account, these values are in sufficient agreement with those from SEM and DLS analysis. Altogether, IZO and IZO particles appear to be practically non-agglomerated.

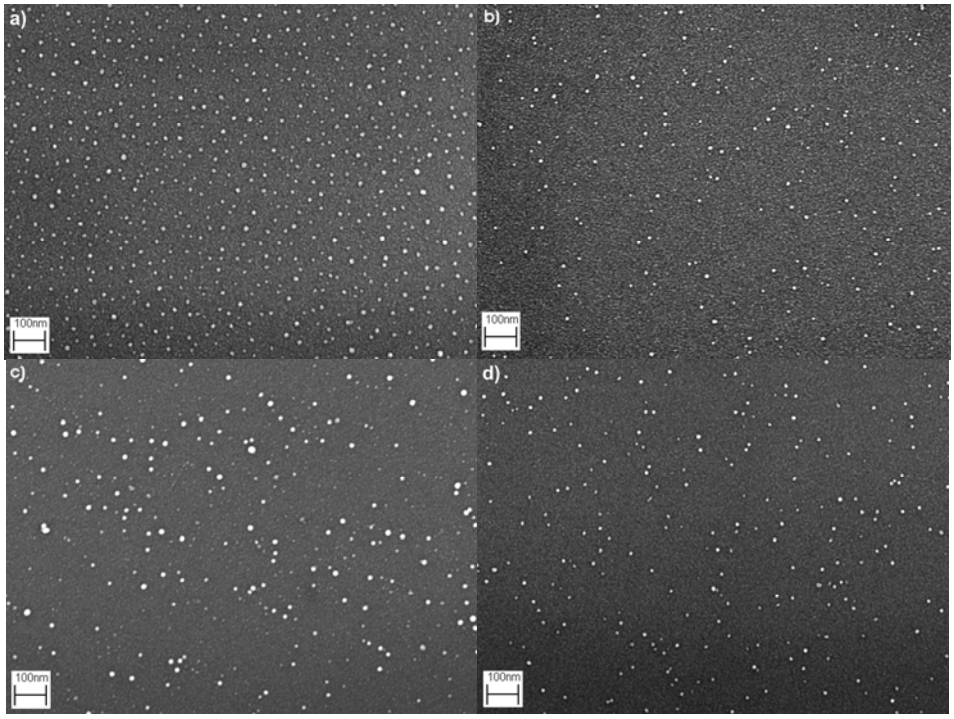


**Figure 7.** SEM images of as-prepared nanocrystals of a) IZO-1, b) AZO-1, c) IZO-2 and d) AZO-2.

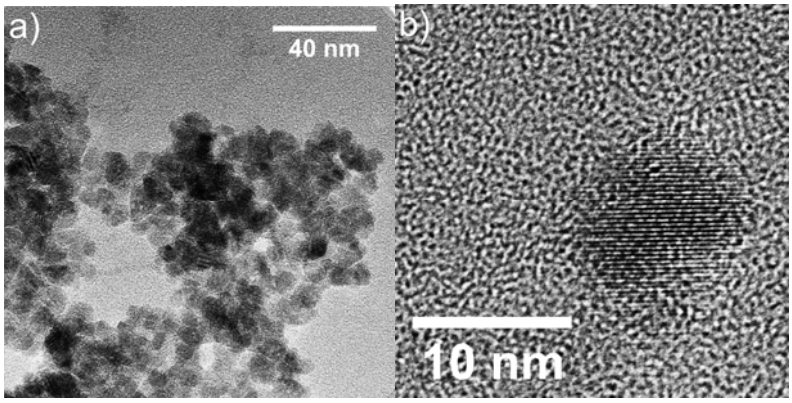


**Figure 8.** TEM images of as-prepared IZO nanocrystals**.**

Transmission electron microscopy (TEM) investigations were performed with IZO and AZO redispersed in ethanol without adding any additional surface-active agent. Characteristic TEM overview images (Fig. 8a) show homogenous, but agglomerated IZO particles with a diameter around 10 nm. High-resolution TEM images show nanoparticles with highly ordered lattice fringes, indicating that even areas close to the particle surface are well crystallized (Fig. 8b). From this image, a lattice plane distance of 2.84±0.08 Å was identified. This distance agrees well with the lattice plane (100) of hexagonal ZnO (2.81 Å).[27] Furthermore, the crystallinity of as-prepared IZO and AZO is confirmed by X-ray diffraction (XRD). Powder diffraction patterns are in accordance with the hexagonal wurtzite-type structure and prove the phase purity of as-prepared nanocrystals [27]. Considering the comparably broad Bragg peaks of the nanoparticles, a significant peak shift is neither expected nor observed although the radii of the lattice constituents and the dopants are different (r($Zn^{2+}$): 0.74 Å; r($Al^{3+}$): 0.54 Å; r($In^{3+}$): 0.80 Å). Nevertheless, the peak width can also be used to calculate the crystallite size via Scherrer's equation. From the most intensive Bragg peaks (100) and (101), an average crystallite size of 8 nm and 12 nm was obtained for IZO-1 and AZO-1,

respectively. Taking all data addressing the particle diameter into account − namely DLS, SEM, TEM and XRD analysis − the uniformity and the low degree of agglomeration of as-prepared IZO and AZO particles are well confirmed, altogether.

To confirm the presence and amount of dopants, as-prepared powders were pressed to pellets and used to perform EDX analysis. This resulted in an In:Zn molar ratio of 6 % for IZO and an Al:Zn molar ratio of 3 % for AZO. Although EDX is not very precise for low amounts of elements incorporated in a sample, the presence of dopants is evidenced with about the same amount as introduced in the synthesis. To validate the incorporation of the dopants in the host lattice, furthermore, electrical measurements via four-point probing were carried out. Again, as-prepared powders were pressed to pellets to reduce the influence of grain boundaries and to initiate a close interparticulate contact. Nevertheless, pellets of as-prepared IZO and AZO showed sheet resistivities in the $M\Omega_{\square}$ range although the particles are highly crystalline and − taking the bluish color into account − free charge carriers seem to be present. However, DEG which is adhered on the particle surface as a stabilizer might hinder the interparticular electron transfer and therefore cause a low conductivity. In fact, several studies aiming at a polyol-mediated synthesis have reported the nanomaterials to contain the multidentate alcohol in quantities of a monolayer even in washed and dried powder materials.[28,29]

In order to illumine the surface conditioning of as-prepared IZO and AZO, FT-IR spectra as well as TG data were recorded. Indeed DEG is indicated by weak vibrations below 1500 $cm^{-1}$ ($\nu$(C−O), $\delta(CH_2)$). An additional vibration around 500 $cm^{-1}$ is ascribed to phonon absorptions of the ZnO lattice.[28–30] Between 4000 $cm^{-1}$ and 1500 $cm^{-1}$ IR-transmission is low due to free charge carriers. TG analysis of IZO and AZO shows a certain weight loss between 200 and 400 °C for both samples. This amounts to 5.3 % for IZO and 2.6 % for AZO and can be related to DEG.[28,29] Thus, about the double amount of DEG is adhered to the surface of IZO particles. This observation is in accordance to the low degree of agglomeration in IZO suspensions. Interestingly, IZO as well as AZO exhibit a much larger amount of DEG adhered to the surface in comparison to our previous results addressing ITO nanocrystals. In contrast to doped ZnO, ITO − gained via very similar measures − also shows an excellent conductivity immediately after synthesis. Finally, Zeta-potential measurements were conducted to verify surface conditioning and colloidal properties of as-prepared IZO and AZO. To this end, the powders were redispersed in water and titrated from neutral pH-range to alkaline and back to acidic pH by addition of NaOH and HCl. As a result, isoelectric points (IEP) of 8.9 for IZO and 8.5 for AZO were deduced. These values are close to the IEP of non-doped ZnO (around pH 9).[31] Thus, the IEP is only weakly affected by doping; only the more acidic $Al^{3+}$ seems to shift the IEP to a lower pH. Right after redispersion, aqueous IZO and AZO suspensions show pH values of 7.2 and 7.5. Since these values are rather close to the IEP, water-based suspensions are of limited colloidal stability (up to some hours).

Aiming at conductive IZO and AZO, as-prepared samples were treated thermally in order to, first, burn-out DEG in air and, second, to re-establish charge carriers by forming gas processing. Since TG analysis showed DEG to be removed below 400 °C, this temperature was chosen for oxidative treatment. After heating in air at 400 °C for 30 min, powders were reduced in forming gas for 60 min at the same temperature. Subsequent to this treatment, FT-IR spectra of AZO show DEG to be absent and the transmittance to be decreased. Furthermore, after reduction with forming gas IZO and AZO pellets show a bright blue color and a sheet resistivity of now 60 $\Omega_{\square}$ and 170 $\Omega_{\square}$, respectively. Considering a pellet thickness of 34 µm, this corresponds to specific resistivities of $2.0 \cdot 10^{-1}$ Ωcm and $5.7 \cdot 10^{-1}$ Ωcm for IZO and AZO. In order to verify the potential influence of a temperature-induced crystallization and particle growth on the electrical properties, the crystallite size of all samples was validated from X-ray powder diffraction patterns via the Scherrer equation. In the case of IZO-2 crystallite sizes of 14 nm (as-prepared), 19 nm (400 °C / 30 min / air) and 18.0 nm (400 °C / 60 min / forming gas) were obtained. A very similar situation persisted for AZO-2: 12 nm (as-prepared), 16 nm (400 °C / 30 min / air) and 16 nm (400 °C / 60 min / forming

gas). Altogether, the crystallite size turned out to be more or less unaffected by the applied thermal treatment. Consequently, the increase in conductivity has to be attributed to improved particle-to-particle contacts subsequent to the oxidative and reductive treatment. This view is further evidenced by non-doped ZnO, which is thermally treated likewise as a reference, and which does not show any measurable conductivity at all.

For optical characterization, the reflectance of IZO, AZO as well as non-doped ZnO powders was measured via UV-VIS spectroscopy (Fig. 9a). Based on these spectra the bandgap was calculated as the energy corresponding to the wavelength where the first derivative of the reflectance is at maximum.[32,33] For non-doped ZnO, this resulted in a wavelength of 383 nm, and a bandgap energy of 3.24 eV (Fig. 9b). This is in accordance with values obtained by other groups using reflectance measurements to determine the bandgap.[32,33] For as-prepared IZO and AZO, bandgap energies of 2.95 eV and 3.18 eV were deduced (Fig. 9b). While heating in air the bandgaps are decreased to 2.85 eV (IZO) and 2.91 eV (AZO). After forming gas process, the bandgap with 3.17 eV for both samples exceeds even the value of the as-prepared materials. Thus, a bandgap shift of +0.3 eV between insulating oxidized samples and conductive reduced samples occurs. This finding is in accordance with the expectation and ascribed to the higher concentration of free charge carriers in reduced samples. The resulting partial filling of the conductance band is well-known as the Moss-Burnstein effect.[34,35] In fact, in comparison to non-doped ZnO, even a larger bandgap energy of the doped samples would have been expected. Thus, a bandgap as large as 3.7 eV has been reported for AZO by some groups utilizing gas-phase deposition methods.[36,37] For nanocrystalline sol-gel AZO samples, bandgaps of 3.3−3.5 eV have been reported. For IZO, bandgaps of 3.3−3.5 eV have been reported for sol-gel as well as for gas-phase deposition synthesis.[38,39] However, all these results are based on transmission measurements of thin layers, which might not directly compare to the diffuse reflectance of powders recorded here.

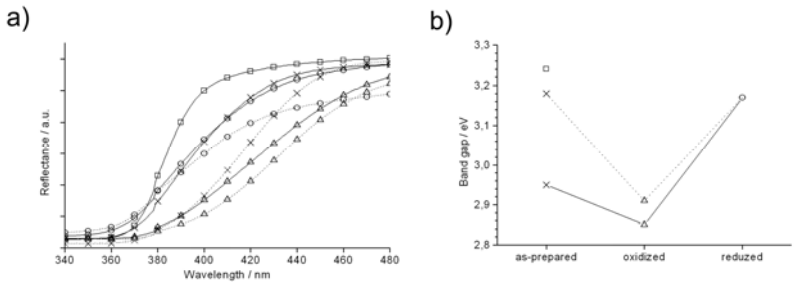


**Figure 9.** a) UV-VIS spectra and b) bandgap energy of powders of AZO (solid), IZO (dotted); as-prepared (cross), after annealing in air (400 °C, 30 min, triangle) and after forming gas process (400 °C, 60 min, circle) in comparison to as-prepared ZnO (square).

As a proof of the concept, IZO and AZO suspensions with solid contents of 10 wt-% were spin-coated on glass plates without any further optimization of, for instance, viscosity, solids content, type of solvent, or substrate preconditioning. In order to increase the particle-to-particle contact as well as the conductivity, as-deposited films were firstly treated thermally in air (500 °C, 1 h), and secondly treated with forming gas ($N_2$:$H_2$ = 90:10, 500 °C, 2 h). SEM images show such post-treated films to be quite homogenous. IZO and AZO films exhibited agglomerates, 40−60 nm and 70−100 nm in diameter. Four-point probing of these IZO films resulted in a sheet resistance of 2.6 $k\Omega_{\square}$. With a film thickness of 800 nm (estimated from SEM images) a specific resistivity of $2.1 \cdot 10^{-1}$ Ωcm is gained without applying any correction factor for porosity. Thus, for IZO the resistivity of post-treated powder pellets and thin films is very similar. While synthesis and resistivity of IZO samples are very reproducible, AZO as a thin film showed a significant variance

in its electrical properties. Best results were obtained when increasing the Al:Zn ratio to 20 % in synthesis. With thin films made from these suspensions, a sheet resistivity of 3.2 $k\Omega_{\square}$ and a specific resistivity ($2.6 \cdot 10^{-1}$ Ωcm) could be gained. The obvious difficulties in the case of AZO are ascribed to the large difference in ionic radii: $r(Zn^{2+})$: 0.74 Å; $r(Al^{3+})$: 0.54 Å. As a consequence, incorporation of $Al^{3+}$ into the ZnO lattice is more difficult and can be incomplete, depending on slight variations of the experimental conditions (e.g., exact temperature at solutions, precursor addition and nucleation; exact concentration of precursors and solvents; exact temperature, placement of crucibles and gas flow velocity inside the furnace during thermal post-treatment). Altogether, nanocrystalline IZO and AZO samples show a high conductivity.

Beside the electrical properties of IZO and AZO thin films, UV-VIS spectra of conductive films on glass plates were recorded to determine its optical properties. Considering a non-optimized film quality, the transmittance in the visible wavelength interval is comparably high: namely 79.7 % for IZO and 77.1 % for AZO (both at 550 nm and with a transmittance of the uncoated glass plate of 91.3 %). The optical absorption coefficient $\alpha$ was calculated from transmission spectra using the relation given by Lambert-Beer's law: $T = exp(-\alpha d)$ (with $T$ as transmittance and $d$ as thickness of the sample). The bandgap energy $E_g$ was then estimated with the assumption of a direct bandgap and the equation given by Tauc *et al.*: $\alpha h\upsilon = A(h\upsilon - E_g)^{1/2}$ (with $A$ as a constant and $h\upsilon$ as the energy at a given wavelength).[40] Extrapolating the linear part of the curves $(\alpha h\upsilon)^2$ as a function of the energy $h\upsilon$ to intercept the energy axis (at $\alpha = 0$.) resulted in bandgap energies of 3.27 eV (IZO thin film) and 3.29 eV (AZO thin film). These values are higher compared to those values stemming from measuring diffuse reflectance of powders, and are indeed in good agreement with literature data of IZO and AZO thin films.[36–41]

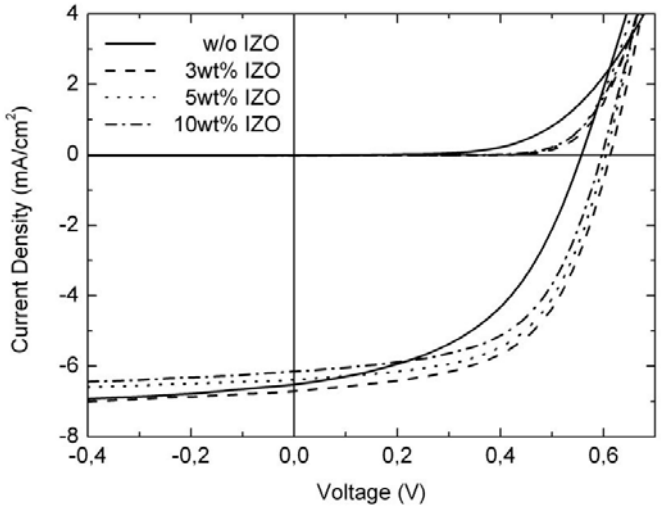


**Figure 10.** Solar cells comprising IZO nanoparticle layers spincoated from different wt-% ethanol solutions. The efficiency of the organic solar cells increases upon the incorporation of an IZO buffer layer mainly due to an enhanced $V_{oc}$ and fill factor. However, the efficiency of the cells slightly decreases with higher concentrated nanoparticle solutions since thicker IZO layers increase the serial resistance of the cells.

Monodisperse, indium doped zinc oxide (IZO) nanoparticles prepared via the polyol-mediated synthesis were incorporated into regular and inverted organic photovoltaic devices as buffer layers below the cathode. Efficient hole blocking at the particle buffer layers leads to an enhanced open circuit voltage of the solar cells. This effect is even more pronounced for inverted device architectures. Device degradation studies revealed a solar cell performance reduction upon sample exposition to ambient atmosphere. However, this degradation is fully reversible under UV illumination. In addition, the n-doped IZO particles form suitable charge carrier transport layers for an efficient recombination in an intermediate recombination zone in tandem solar cells. Accordingly we have fabricated fully solution processed tandem solar cells and investigated their optoelectronic properties (Figure 10, Figure 11).

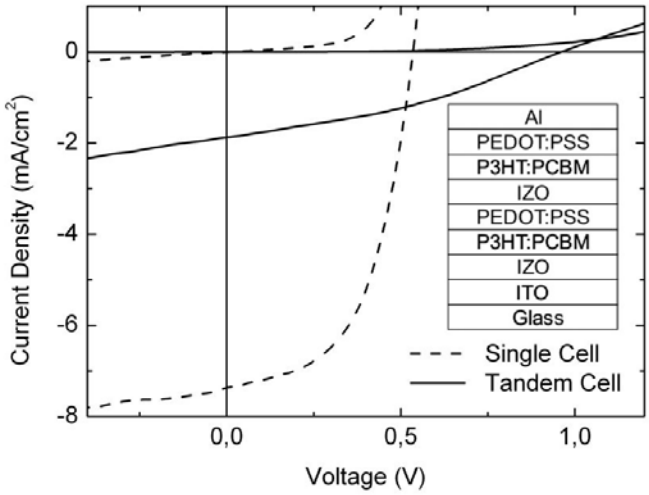


**Figure 11.** JV curves of a solution processed tandem solar cell comprising two absorbing P3HT:PCBM layers. The open circuit voltage of 1150 mV indicates a proper working device. For comparison the JV characteristics of an inverted single cell are given.

### 3. Doped tin oxide (FTO)

Liquid-phase preparation of nanoscaled $SnO_2$:F (FTO) so far has been performed by utilizing sol-gel methods. There resistivities of 0.7−0.8 Ωcm were achieved for powders. Moreover, resistivities of 0.1−1 Ωcm have been reported for sol-gel made thin-films. Unfortunately, data regarding particle size and size distribution in the liquid-phase have not been reported. Based on our knowledge on preparing nanoscaled TCO materials via a polyol-mediated synthesis, this method was selected to realize nanoscaled FTO, too. The polyol − i.e., a multidendate high-boiling alcohol such as glycerol, ethylene glycol or diethylene glycol − allows for efficient control of nucleation and growth of nanoparticles. Thus, the size of the nanoparticles can be controlled and their agglomeration suppressed. Moreover, crystalline nanoparticles can be gained due to the high boiling-point of the polyols.

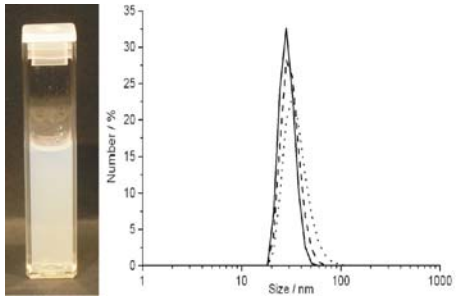


**Figure 12.** Left: photograph of FTO-ap (0.4 mol-%) nanoparticles in a cuvette; right: particle size distribution of FTO-ap (0.4 mol-%) in DEG according to DLS analysis: as-prepared suspension (solid), FTO-ap powder redispersed in DEG (dashed), and FTO-ap powder redispersed in EtOH (dotted).

Here, $SnO_2$:F (FTO) nanoparticles with different doping levels were prepared in diethylene glycol (DEG) as the polyol. Heating was performed via microwave irradiation, which turned out to be beneficial for optimized particle size and improved materials crystallinity. As-prepared FTO (indicated as FTO-ap) suspensions exhibit a slightly bluish appearance (Figure 12). EDX confirms the presence of fluorine in FTO-ap. However, the accuracy of the method is limited for light elements. Therefore, quantitative analysis was performed by wet-chemical analysis and resulted in 0.4 mol-% and 1.2 mol-% and are therefore indicated as FTO-ap (0.4 mol-%) and FTO-ap (1.2 mol-%) in the following. Thus, the fluorine content is significantly lower than compared to the concentration introduced in the synthesis (i.e. 1 mol-% and 10 mol-%). This finding is ascribed to the very high solubility of $N(CH_3)_4F \cdot 4\ H_2O$ as the fluorine precursor so that major amounts of fluorine remain in solution. Nevertheless, the incorporation of fluorine is valuably evidenced. Note also that such a quantitative analysis of the dopant content is lacking in literature most often.

According to scanning electron microscopy (SEM), FTO-ap exhibits a spherical shape with a uniform morphology (Figure 13). Some aggregates of several nanoparticles that are observed on overview-SEM images stem from the drying process when preparing the specimen for electron microscopy. Based on a statistical evaluation of > 200 particles, mean diameters of 15 nm for FTO-ap (0.4 mol-%) and 12 nm for FTO-ap (1.2 mol-%) were determined. SEM images of FTO-ap (0.4 mol-%, 1.2 mol-%) exhibit single crystalline areas of 4 nm in size. With 3.3 Å the distance of the lattice fringes agrees well with $SnO_2$ (cassiterite: (110) with 3.35 Å). These findings indicate that FTO-ap consists of much smaller crystalline domains than one could have assumed from DLS and SEM measurements which indicates that FTO-ap are "polycrystalline" nanoparticles as explained in the introduction.

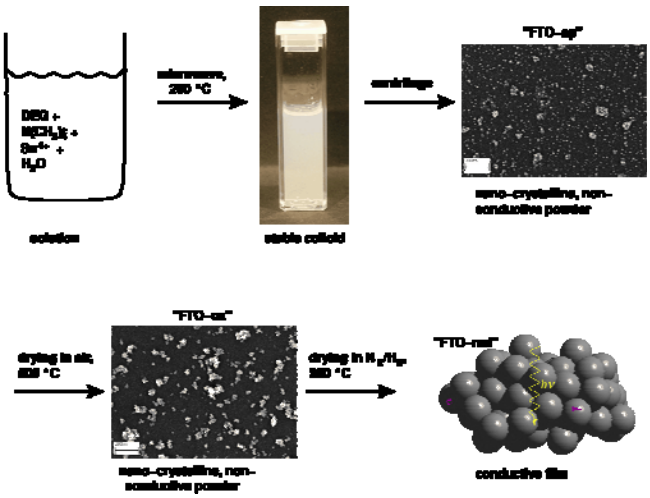


**Figure 13.** Simplified flow-diagram showing synthesis, products and main properties.

To investigate the conductivity of FTO-ap, powder samples were first pressed to pellets. This measure guarantees a close contact between the individual nanoparticles. Thereafter, the pellets were investigated by four-point probing. Accordingly, FTO-ap samples did not show any measurable conductivity. Aiming at conductive materials, FTO-ap was thermally treated in order to, first, remove residual DEG and water, and second, diminish grain boundaries between different monocrystalline domains. With regard to TG analysis, as-prepared FTO was therefore annealed under oxidizing conditions in air at 500 °C for 2 h. To differentiate from as-prepared FTO (FTO-ap), these samples heated in air were indicated as FTO-ox-500 in the following. The FTO samples were reductively processed in forming gas at 250 °C for 1 h to establish free charge carriers subsequent to the first oxidative thermal treatment,(FTO-red). Both of these thermal treatments, the oxidative as well as the reductive one are quite typical and often applied to process transparent conductive oxides. To study for further structural and morphological effects, the FTO samples were finally heated in air at 800 °C for 30 min (indicated as FTO-ox-800.

As expected, even non-doped $SnO_2$ (TO-red) shows a remarkable conduction due to oxygen vacancies. Fluorine doping nevertheless results in a significantly reduced resistivity with 13 and 0.2 Ωcm as the lowest values in the case of FTO-red (1.2 mol-%). Comparing these values to literature, the resistivity of the FTO-red (0.4 mol-%) is similar to what was reported on powders gained via the sol-gel method. The resistivity of FTO-red (1.2 mol-%) is even lower and matches sol-gel films prepared by Biswas *et al.* Thus, the polyol method gives an easy access to conductive FTO samples without the need of advanced metal-organic precursors as required for the sol-gel synthesis.

How is fluorine incorporated into the structure of the polycrystalline $SnO_2$ nanoparticles? For $SnO_2$:F deposited in thin layers several structural models are currently discussed[2] that are consistent with Hall effect measurements which give evidence of n-doping. Several point defects can be considered to explain n-doping of $SnO_2$:F. Provided that charge neutrality is maintained in the particles, only defects representing a positive charge relative to the host structure $SnO_2$ can introduce excess electrons. The defects are conveniently written in Kröger-Vink notation as follows:

i) oxygen vacancies $V_O^{\bullet\bullet}$ (+ $2e^-$ delocalized)
ii) fluorine filled oxygen vacancies $F_O^{\bullet}$ (+ $e^-$ delocalized)
iii) tin on interstitial sites $Sn_i^{\bullet\bullet\bullet\bullet}$ (+ 4 $e^-$ delocalized)
iv) hydrogen on interstitial sites $H_i^{\bullet}$ (+ $e^-$ delocalized)

Oxygen vacancies are related to oxygen vapor pressure $p(O_2)$ and are generated in pure $SnO_2$ at higher temperatures according to the following defect equilibrium:

$$O_O \rightleftarrows 1/2\ O_2 \uparrow + V_O^{\bullet\bullet} + 2e'$$

For nanoparticles the situation is complicated by the high surface area which is likely to host a variety of chemical environments of tin, oxygen and fluorine. Also for nanoparticles the charge neutrality criterion applies. However, electrons introduced by doping with different defects may prefer to be localized at the surface rather than increasing the charge carrier concentration in the particle core. A particle core of the composition $Sn(IV)O_{2-x}$ doped with $x$ F should carry a positive charge which would have to be balanced by a negative charge at the particle surface. This process would also limit the size of the nanoparticles and stabilize the colloids. Due to its band structure, $SnO_2$ is able to convey charge from core to shell which is underlined by the DFT calculations presented below (electron difference plots). Clearly it is essential to the electrical conductivity to treat the nanoparticles with a reducing agent after precipitation, i.e. here the forming gas, in order to finally provide the electrons for n-doping. How is structure related to electrical resistivity?

Several factors contribute to the observed bulk resistivity. Important are the charge carrier concentration, grain boundary scattering, lattice vibrations and ionized impurity scattering. An optimum conductivity exists because the charge carrier concentration will decrease resistivity and the scattering at ionic defects will increase resistivity with increasing F doping. Literature values

obtained on $SnO_2$:F films indicate that ideal behavior is reached around 6-8 wt % for fluorine doping. Next to doping also treatment with different gases may influence the charge carrier concentration. In our case, treatment of the nanoparticles with forming gas, at elevated temperatures will increase the number of oxygen vacancies. The nanoscale structure of the prepared $SnO_2$:F adds further factors which influence electrical resistivity. The charge carrier concentration may be lower than expected because electrons introduced by doping are localized at the surface of the nanoparticles[2] and not, as intended, delocalized in the $SnO_2$ conduction band. Furthermore the grain-boundaries between different nanoparticles will contribute to resistivity. The purpose of the magnetic resonance techniques below is to shade some light onto the role of fluorine doping in this case. Important issues are to find out if F atoms prefer the shell or are rather homogeneously doped into the $SnO_2$ particles and in which environments/site F atoms are located. By solid-state NMR, the $SnO_2$ host, the nanoparticle interfaces, and the environments of the doped F-atoms can be studied. In the following we start first with the findings from 1D experiments ($^{119}$Sn, $^{19}$F). Then we probe the homogeneity of F-doping with homonuclear recoupling experiments and finally we determine constraints for F-Sn or H-F distances by REDOR experiments.

In Figure 14 we sketch out a model for as-prepared $SnO_2$:F particles (FTO-ap) which is consistent with the aforementioned observations. The as-prepared $SnO_2$:F nanoparticles are polycrystalline. Their mono-crystalline domains are approximately 2-4 nm in diameter (TEM, XRD and $^{119}$Sn{$^1$H} C-REDOR-NMR). At the boundaries between different mono-crystalline regions hydrogen atoms accumulate and fill the voids ($^{119}$Sn{$^1$H} C-REDOR-NMR). F-atoms fill O-vacancies in the host structure (quantum chemical calculations, $^{119}$Sn{$^{19}$F}-CP-NMR) and do no exhibit clustering ($^{19}$F-$^{19}$F 2D NMR correlation spectroscopy), still the distribution of F-atoms is not completely random and shows a preference to the intraparticle surfaces (comparison of $^{119}$Sn{$^1$H} C-REDOR and $^{19}$F{$^1$H} C-REDOR-NMR). The electrons contributed by F-doping are localized at the intraparticle surface possibly in form of ionized surface defects (quantitative $^{119}$Sn NMR and $^{119}$Sn Mößbauer spectroscopy).

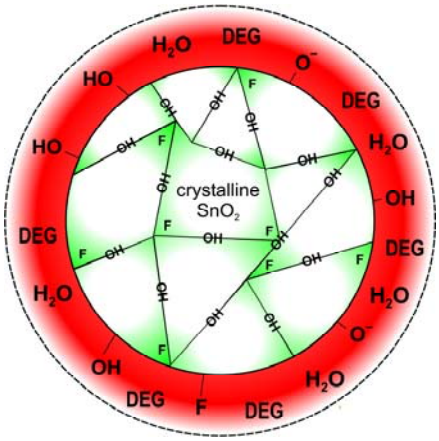


**Figure 14.** Model of polycrystalline FTO-ap nanoparticle; within the $SnO_2$ crystallites $F^-$ ions are inserted on oxygen sites (dark shading indicates a higher doping concentration near the grain boundaries); the charge is compensated at the intraparticle and outer surfaces; the latter is covered by a solvent layer consisting of DEG and water.

## 4. Doped tin oxide as a photocatalyst

Two major challenges of the 21st century will be the shortage of energy supplies and water scarcity.[42,43] Photocatalysis could basically be the answer to both problems. Often referred to as "green" technology, it has the ability to split water, to decompose organic pollutants and to crucify

germs.[44,45] The latter two aspects could be used for detoxification of waste water and for providing potable water. Since its excellent photocatalytic properties were reported in 1972,[46] the prime example is still $TiO_2$ (anatase) as it is available in large quantities at low-cost, too. On the other hand, $TiO_2$ – like many other metal oxides – has to be activated by UV-illumination and is rather inactive under visible light due to its large band gap (3.2 eV).[47] Since the solar spectrum contains only a small portion of UV-light, a photocatalyst that works efficiently under daylight would be much more purposeful.

In recent years, there have been many attempts to realize efficient visible-light-sensitive photocatalysts.[44-48] And numerous catalysts that show a response to visible light have been published in the mean time including $AgNbO_3$[49], $InNbO_3$[50], $CaBi_2O_4$[51], $BiSbO_4$ [52], $Bi_2WO_6$ [53-55], or $BiVO_4$.[56-58] Since many of these compounds include harmful and/or high-cost elements, its technical mass application might be restricted. Theoretical considerations indicate that $SnWO_4$ could be an excellent visible-light-sensitive photocatalyst, too.[59] Surprisingly, this compound has received little attention so far. As firstly reported by *Jeitschko* and *Sleight*, the *n*-type semiconductor $SnWO_4$ exists in a low-temperature dark-red α- and a high-temperature bright-yellow β-phase.[60,61] The band gaps were determined experimentally to 1.6 eV and 2.2 eV, respectively.[62] Both phases have been prepared by solid state reactions as bulk materials.[60-62] On the nanoscale, only the dark red α-phase has been yet prepared via a hydrothermal approach.[63] In the following, a quick and easy, water-based room-temperature synthesis – and thereby named real "green" synthesis – of high-surface yellow β-$SnWO_4$ nanoparticles containing a certain amount of α-Sn is reported.[64] The colloidal, structural and morphological properties of the nanoparticles are evaluated and the very promising daylight-driven photocatalysis is demonstrated.

The title compound β-$Sn_{1-n}WO_4$ · n α-Sn is prepared by a most simple precipitation in neutral water at room-temperature. The synthesis is quick and easy; harmful elements or solvents are not required. Based on these experimental conditions, the synthesis can be denoted as real "green".[64] Although the synthesis is very easy to perform, the size of the nanoparticles as well as their size distribution is of very high quality. Note further that β-$Sn_{1-n}WO_4$ · n α-Sn reproducibly contains α-Sn with a fixed concentration (see below). Phase separation obviously occurs instantaneously while performing the synthesis and reflects the initial 1:1 ratio of Sn and W as introduced into the reaction.

Small sized particles are crucial for a highly efficient photocatalyst for two reasons: First, light-generated electron–hole pairs in nanomaterials exhibit shorter diffusion paths to the surface and face fewer recombination sites. Secondly, the photocatalytic activity is closely correlated to the available specific surface of the catalyst. With regard to as-prepared $Sn_{1-n}WO_4$ · n α-Sn, the particle size was evaluated by differential sedimentation (DS) and dynamic light scattering (DLS) (Fig. 15a). Accordingly, DS results in a mean diameter of 17 nm and a narrow size distribution. The hydrodynamic diameter as obtained by DLS is – as expected – sligthly larger (22 nm).

Scanning electron microscopy (SEM) confirms the narrow size distribution of as-prepared $Sn_{1-n}WO_4$ · n α-Sn (Fig. 15a). Statistical evaluation based on about 1000 particles results a mean diameter of 13 nm. Finally, the specific surface of as-prepared $Sn_{1-n}WO_4$ · n α-Sn was determined to 71±1 $m^2 g^{-1}$. Note that this value is superior to those of the mostly applied anatase reference (Degussa P25: 50 $m^2 g^{-1}$) as well as to many other visible-light-sensitive catalysts reported so far.[44,45,57,65] Aiming at $SnWO_4$, the photocatalytic properties have been to date only tested on bulk material with a specific surface as low as 3 $m^2 g^{-1}$.[62] Assuming non-porous nanoparticles and considering the bulk density of β-$SnWO_4$ (7.43 g $cm^{-3}$),[60] a mean particle diameter of 11 nm can be derived from the specific surface, which – together with values stemming from DS, DLS and SEM – confirms the uniformity and the low degree of agglomeration of as-prepared $Sn_{1-n}WO_4$ · n α-Sn.

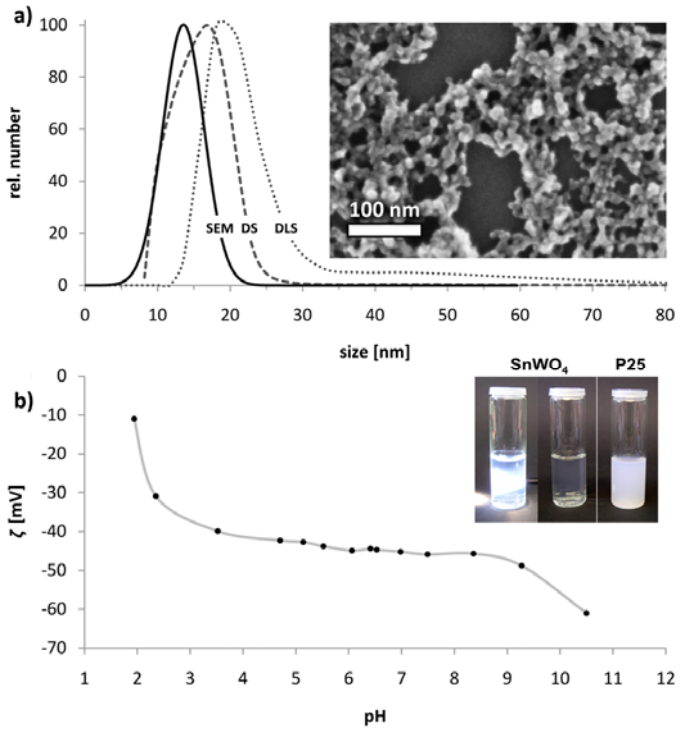


**Figure 15.** Colloidal properties of as-prepared β-$Sn_{1-n}WO_4$ · n α-Sn nanoparticles: a) Size distribution of $SnWO_4$-nanoparticles in aqueous suspension determined with statistical evaluation of scanning electron microscopy images (SEM), differential sedimentation (DS) and dynamic light scattering (DLS). A representative SEM image is shown, too; b) ζ-potential as a function of pH and photographs of aqueous suspensions (0.01 wt-%, neutral pH) of as-prepared $SnWO_4$ nanoparticles (with and without Tyndall light cone) and an aqueous suspension (0.01 wt-%, neutral pH) of Degussa P25 for comparison.

In addition to a small size, a sufficient colloidal stabilization is relevant for the purpose of photocatalysis in liquid/aqueous media to exclude any reduction of the specific surface due to agglomeration processes. Since stabilizing capping agents do not only cover a significant part of the particle's surface but are also affected by photocatalytic decomposition themselves, only electrostatic stabilization can provide a long-term stability of the nanoparticles resulting in a lasting high catalytic performance. Thus, the surface charge of as-prepared $Sn_{1-n}WO_4$ · n α-Sn was quantified by pH-controlled zeta-potential measurements (Fig. 15b). The nanoparticles exhibit a negative zeta-potential with constant, high surface charges ($\zeta < -40$ mV) over a wide pH-range (3.5 – 9.5). With these features the material exceeds those found for Degussa P25[68] or $BiVO_4$[57]. Dissolution of the nanoparticles is only observed in both, strongly alkaline and acidic milieu (pH < 2.5, pH > 10). Hence, fairly stable aqueous suspensions of as-prepared $Sn_{1-n}WO_4$ · n α-Sn can be achieved not only in neutral water but also in moderate alkaline and acidic milieu, which is highly advantageous with respect to an application in wastewater treatment. Because of its high surface charge, $Sn_{1-n}WO_4$ · n α-Sn shows excellent colloidal stability in water. Considering the similar size of commercial $TiO_2$ (Degussa P25) and as-prepared $Sn_{1-n}WO_4$ · n α-Sn, this becomes obvious when comparing the turbidity of the corresponding suspensions at neutral pH (Fig. 15b).

According to X-ray powder diffraction pattern, the as-prepared nanomaterial exhibits two surprising characteristics: First, the obtained material can be referred to as amorphous tin tungstate just showing an incipient crystallinity. Note however that the broad maximum at around $2\theta = 27$ ° coincides with the most intensive Bragg peak of β-$SnWO_4$. Secondly, a sharp and comparably weak

Bragg peak at $2\theta = 38\,°$ very reproducible points to minor amounts of elemental cubic α-Sn. Despite the presence of elemental tin, energy-dispersive X-ray analysis (EDX) reveals an equimolar ratio of tin and tungsten (Sn:W = 0.97 ± 0.07) and confirms the equimolar Sn(II):W(VI) ratio as introduced to the synthesis. In sum, this points to the presence of an unusual α-Sn-containing, sub-stoichiometric tin tungstate phase as indicated by the formula β-$Sn_{1-n}WO_4$ · n α-Sn. In accordance to these findings, the material transforms to stoichiometric, single-phase α-$SnWO_4$, when tempered in *nitrogen atmosphere*. Note that $SnW_3O_9$ and $SnO_2$ are obtained if the as-prepared β-$Sn_{1-n}WO_4$ · n α-Sn sample was tempered *in air*. Based on the ratio of the X-ray intensities (β-$SnWO_4$:α-Sn) as well as on the amount of $SnW_3O_9$ and $SnO_2$ the composition of β-$Sn_{1-n}WO_4$ · n α-Sn can be approximated to β-$Sn_{1-n}WO_4$ · n α-Sn with n = 0.05±3.

Sub-stoichiometric tin tungstate containing a certain amount of cubic α-Sn has not been described, yet. However, the synthesis was performed here at ambient temperature unlike previous routes, which were conducted at elevated temperatures.[63] Although the underlying phase seggregation might be complex in detail, it seems reasonable to assume that a small part of Sn(II) undergoes disproportionation to Sn(0) and Sn(IV), which is an exothermic reaction and therefore favored at low reaction temperatures.[64] In addition, a certain inclusion of Sn(IV) in tungstate phases was reported earlier for $SnWO_4$-based gas sensors as well as for bulk-$SnWO_4$.[62,63] Interestingly, Sn(0) is found in the cubic α-modification of diamond, that is usually stable below 13.2 °C.[69] However, there are many reports on α-Sn exhibiting an anomalous thermal stability when being confined on the nanoregime.[70] Moreover, it is well known that the phase transition β-Sn (tetragonal) → α-Sn (cubic) can be triggered via the presence of materials that crystallize in the cubic crystal system like CdSe or InSb.[71] And β-$SnWO_4$ is with cubic symmetry, too. Hence, it seems possible that the two unusual phases – namely the high temperature phase of β-$SnWO_4$ and the low-temperature phase of α-Sn – promote each other's appearance due to their common crystal system.

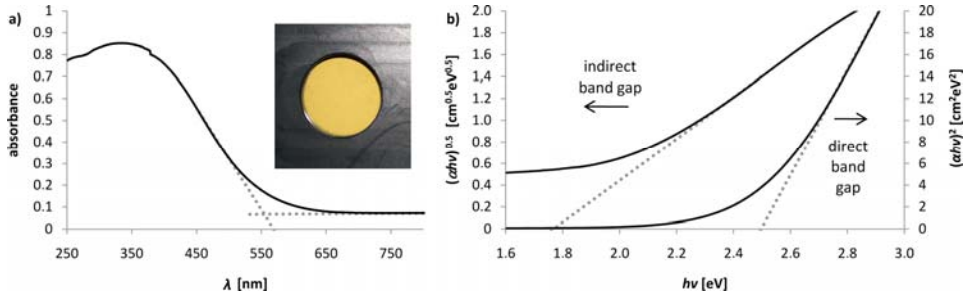


**Figure 16.** UV–VIS spectra and photograph of as-prepared β-$Sn_{1-n}WO_4$ · n α-Sn (a) and optical band gap determination (b).

As may be expected from its bright yellow color, as-prepared β-$Sn_{1-n}WO_4$ · n α-Sn samples exhibit a strong absorption band in the visible spectral range at 554 nm (2.2 eV) (Fig. 16a). This value fits indeed much better to the yellow high-temperature phase of bulk β-$SnWO_4$ (537 nm, 2.3 eV) than to dark red bulk of α-$SnWO_4$ (692 nm, 1.8 eV).[62] Density functional theory (DFT) calculations showed that the valence band of $SnWO_4$ is formed by hybrid orbitals of Sn*5s* and O*2p* in both polymorphs. The conduction band of α-$SnWO_4$ is formed by W*5d* orbitals, whereas Sn*5p*-orbitals contribute to the conduction band of β-$SnWO_4$. The calculations revealed α-$SnWO_4$ and β-$SnWO_4$ to have an indirect and direct band gap respectively. To evaluate the type of band gap of the nanomaterial obtained here, $(\alpha h\nu)^{0.5}$ and $(\alpha h\nu)^2$ versus $h\nu$ plots were analyzed (Fig. 16b) resulting in 1.77 eV if an indirect band gap is assumed and 2.50 eV for the assumption of a direct band gap. The latter value is in almost perfect agreement with the prediction of Lacomba-Peralesel and coworkers for β-$SnWO_4$ (2.52 eV).[72] Furthermore, the absorption edge of 2.2 eV found via diffuse reflectance spectra confirms the assumption of a direct band gap of 2.50 eV. For comparison, DFT calculations

predict 1.9 eV for α-$SnWO_4$ and 2.9 eV for β-$SnWO_4$,[73] whereas Cho *et al.* found 1.64 eV for bulk α-$SnWO_4$ and 2.68 eV for bulk β-$SnWO_4$ experimentally.

The photocatalytic activity of as-prepared β-$Sn_{1-n}WO_4$ · n α-Sn was measured through the degradation of various organic dyes in neutral water under simulated daylight by monitoring the time-dependent decrease of the dye concentration at its maximum of absorption. To this concern, phenothiazine dye methylene blue (MB, $\lambda_{max}$: 664 nm), triphenylmethane dye basic green 4 (BG, $\lambda_{max}$: 617 nm) and azo-dye methyl red (MR, $\lambda_{max}$: 460 nm) were chosen as model substances (Fig. 17). Commercially available Degussa P25 ($TiO_2$, 80 % anatase, 20 % rutile) was used as a standard reference catalyst.[47,48,65-67] Here, the degradation of all dyes was hardly accelerated demonstrating that Degussa P25 is rather inactive under simulated daylight as has been described many times before (Fig. 17a–c).[47,48,65-67,74] On the contrary, as-prepared β-$Sn_{1-n}WO_4$ · n α-Sn displayed significant decomposition of all tested dyes with 5–10 times higher degradation rates (Tab. 1), when used in equal molar concentration as Degussa P25 under the same conditions. A blank sample of MR was almost fadeless under irradiation, demonstrating a typical feature of azo-dyes, whereas MB showed self-photosensitized photolysis to a certain degree, due to the small proportion of UV-light (approximately 3 %) in the lamp spectrum. Altogether, the efficient photocatalytic performance of nanoscaled, incipient-crystalline β-$Sn_{1-n}WO_4$ · n α-Sn is first observed and will certainly occur for many other organic contaminants, too.

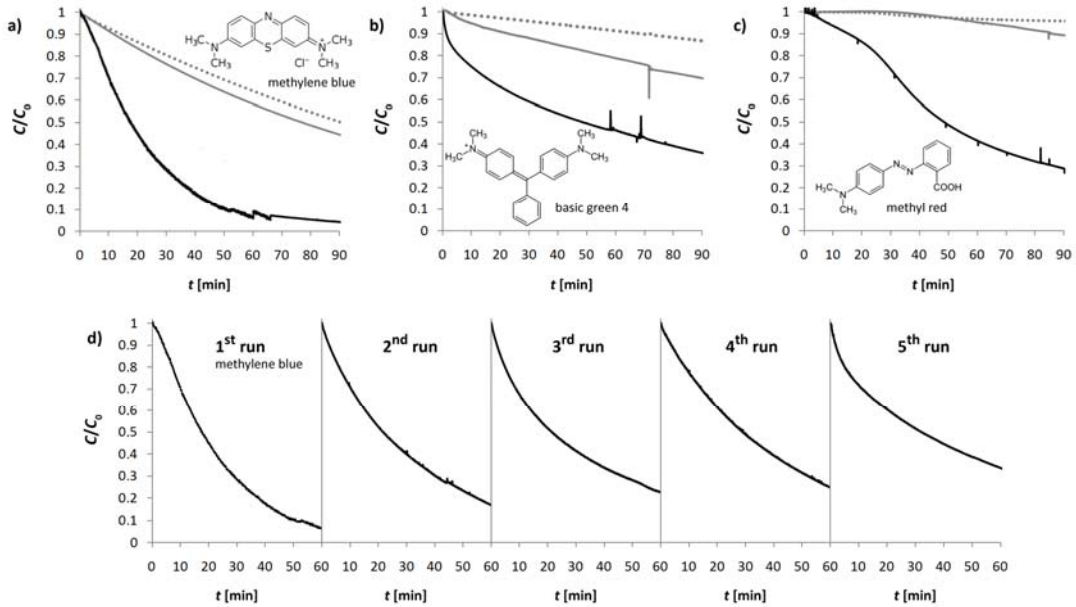


**Figure 17.** Photocatalytic degradation of a) MB, b) BG, c) MR, and d) MB in recycling experiments under simulated daylight. Degradation catalyzed by Degussa P25 (grey line) and as-prepared β-$Sn_{1-n}WO_4$ · n α-Sn (black line) is shown for equimolar concentration ($1.25 \cdot 10^{-3}$ M). Dotted lines represent blank dyes irradiated without any catalyst. Spikes and sudden offsets are caused by air bubbles passing the flow-through cuvette. Dye concentrations were $2 \cdot 10^{-5}$ M for MB and BG, whereas MR was used in a 1:5 diluted saturated solution ($\leq 2 \cdot 10^{-5}$ M) due to its low solubility.

The reusability of as-prepared β-$Sn_{1-n}WO_4$ · n α-Sn nanoparticles was addressed in recycling experiments. After a given time-interval, 0.5 mL of a comparatively highly concentrated MB-solution ($1 \cdot 10^{-3}$ M) was injected into the batch to restore the initial MB-concentration ($2 \cdot 10^{-5}$ M) while leaving the overall volume almost unchanged. Degradation products of MB were not removed and are expected to cause surface contamination of the catalyst as was reported earlier. Indeed, after several runs the removed catalyst powder exhibited a violet color. This is probably owing to

adsorbed intermediates that accumulated during the repeated MB degradation, e.g. violet-colored azure B formed by *N*-demethylation of MB. Nonetheless, the activity of the catalyst is only slightly reduced after several runs proving the recyclability of as-prepared β-$Sn_{1-n}WO_4$ · n α-Sn nanoparticles (Fig. 17d). Note that XRD pattern of the catalyst that were recorded after several photocatalytic cycles do not exhibit a significant change as compared to the as-prepared material – including the incipient-crystalline β-$SnWO_4$ phase as well as the Bragg peak of α-Sn. Both findings indicate that β-$Sn_{1-n}WO_4$ · n α-Sn as a photocatalyst remains intact and that Sn(0) is not consumed during the reaction.

The role of Sn(0) in the photocatalytic process remains unclear at this point. It is conceivable that exposed Sn atoms provide favorable binding sites for pollutant molecules (e.g. S-type lone-pairs of MB). Besides that, in many composite photocatalysts heterojunctions were described to be beneficial for the photocatalytic performance. Using the method described by Wang *et al.*,[75] the top of the valence band of α-Sn is to be expected at higher energy than the valence band edge of $SnWO_4$. Taken this assumption for granted, photogenerated holes are supposed to be transferred quickly to Sn(0) and thereby separated from the electrons. In that way, direct recombination of photogenerated carriers could efficiently inhibited, resulting in an enhanced photocatalytic performance. Nonetheless, further studies are needed to elucidate the role of Sn(0) and the non-stoichiometry of the β-$SnWO_4$ lattice. The very promising photocatalytic activity of the complex phase β-$Sn_{1-n}WO_4$ · n α-Sn is nevertheless reliably proven and very reproducible.

A final quantification of the photocatalytic activity of as-prepared β-$Sn_{1-n}WO_4$ · n α-Sn in comparison to other photocatalysts is difficult since several constraints have been barely addressed in many studies. This includes the use of more than one dye, the role of leuco-forms, the need of recycling studies, the application of simulated daylight instead of UV- or blue light as well as experimental conditions that differ in detail. β-$Sn_{1-n}WO_4$ · n α-Sn, nevertheless, seems to be one of the most efficient photocatalysts under simulated daylight.

## References

*- own work with complete titles -*


[1] D. R. Lide (ed.), *Handbook of Chemistry and Physics*, CRC Press, Boca Raton 2005.
[2] F. Fievet, J.P. Lagier, M. Figlarz, *MRS Bull.* **1989**, *14*, 29.
[3] P Toneguzzo, G. Viau, O. Acher, F. Guillet, E. Bruneton, F. Fievet, *J. Mater. Sci.* **2000**, *35*, 3767.
[4] C. Feldmann, Polyol-mediated Synthesis of Nanoscale Functional Materials, *Adv. Funct. Mater.* **2003**, *13*, 101.
[5] C. Feldmann, C. Metzmacher, Polyol mediated Synthesis of nanoscale Sulfides MS (M = Zn, Cd, Hg), *J. Mater. Chem.* **2001**, *11***,** 2603.
[6] C. Feldmann, M. Roming, K. Trampert, Polyol-mediated Synthesis of Nanoscale $CaF_2$ and $CaF_2$:Ce,Tb, *Small* **2006**, *2*, 1248.
[7] B. L. Cushing, V.L. Kolesnichenko, C.J. O'Connor, *Chem .Rev.* **2004**, *104*, 3893.
[8] I. Pastoriza-Santos, L. M. Liz-Marzan, *Langmuir* **2002**, *18*, 2888.
[9] O. Palchik, R. Kerner, A. Gedanken, A.M. Weiss, M. Slifkin, V. Palchik, *J. Mater. Chem.* **2001**, *11*, 874.
[10] Z. Liu, Z. Sun, B. Han, J. Zhang, J. Huang, J. Du, S. Miao, *J. Nanosci. Nanotechnol.* **2006**, *6*, 175.
[11] Y. Jiang, Y. Zhu, Z. Xu, *Mater, Letters* **2006**, *60*, 2294.
[12] W. Ostwald, *Z. Phys. Chem.* **1879**, *22*, 289.

[13] C. Feldmann, Preparation and Characterisation of Nanoscale Vb-Metal Oxides $M_2O_5$ (M = V, Nb, Ta), *Z. anorg. allg. Chem.* **2004**, *630*, 2473.
[14] C. Feldmann, S. Matschulo, S. Ahlert, Polyol-mediated Synthesis of Nanoscale $Mg(OH)_2$ and MgO, *J. Mater. Sci.* **2007**, *42*, 7076.
[15] I. Hamberg, C. G. Granqvist, *Appl. Opt.* **1985**, *24*, 1815.
[16] L. B. Valdes, Proceedings IRE 40 (1952) 445.
[17] F. Fievet, J. P. Lagier, M. Figlarz, Mater. Res. Soc. Bull. 14 (1989) 29.
[18] P. Toneguzzo, G. Viau, O. Acher, F. Guillet, E. Bruneton, F. Fievet, J. Mater. Sci. 35 (2000) 3767.
[19] C. Feldmann, H. O. Jungk, Polyol-mediated Preparation of nanoscale Oxide Particles, Angew. Chem. Int. Ed. 40 (2001) 359.
[20] C. Feldmann, M. Roming, K. Trampert, Polyol-mediated Synthesis of Nanoscale $CaF_2$ and $CaF_2$:Ce,Tb, Small 2 (2006) 1248.
[21] A. Müller, O. Heim, M. Panneerselvam, M. Willert-Porada, Mater. Sci. Bull. 40 (2005) 2153.
[22] O. Palachik, J. Zhu, A. Gedanken, J. Mater. Chem. 10 (2000) 1251.
[23] B. L. Cushing, V. L. Kolesnichenko, C. J. O'Connor, Chem. Rev. 104 (2004) 3893.
[24] I. Pastoriza-Santos, L. M. Liz-Marzan, Langmuir 18 (2002) 2888.
[25] O. Palchik, R. Kerner, A. Gedanken, A. M. Weiss, M. Slifkin, V. Palchik, J. Mater. Chem. 11 (2001) 874.
[26] Z. Liu, Z. Sun, B. Han, J. Zhang, J. Huang, J. Du, S. Miao., J. Nanosci. Nanotechnol. 6 (2006) 175.
[27] Y. Jiang, Y. Zhu, Z. Xu, Mater. Lett. 60 (2006) 2294.
[28] W. Bragg, Philos. Mag. 39 (1920) 647.
[29] C. Feldmann, Preparation and Characterisation of Nanoscale Vb-Metal Oxides $M_2O_5$ (M = V, Nb, Ta), Z. anorg. allg. Chem. 630 (2004) 2473.
[30] C. Feldmann, S. Matschulo, S. Ahlert, Polyol-mediated Synthesis of Nanoscale $Mg(OH)_2$ and MgO, J. Mater. Sci. 42 (2007) 7076.
[31] P. Y. Emelie, J. D. Phillips, B. Buller, U. D. Venkateswaran, J. Electron. Mater. 35 (2006) 525.
[32] G. A. Parks, Chem. Rev. 65 (1965) 177.
[33] R. E. Marotti, P. Giorni, G. Machado, E. A. Dalchiele, Sol. Energy Mater. Sol. Cells 90 (2006) 2356.
[34] T. Ren, H. R. Baker, K. M. Poduska, Thin Solid Films 515 (2007) 7976.
[35] E. Burnstein, Phys. Rev. 93 (1954) 632.
[36] T. S. Moss, Proc. Phys. Soc. B 67 (1954) 775.
[37] Z. Q. Li, D. X. Zhang, J. J. Lin, J. Appl. Phys. 99 (2006) 124906.
[38] R. K. Shukla, A. Srivastava, K. C. Dubey, J. Cryst. Growth 294 (2006) 427.
[39] G. Machado, D. N. Guerra, D. Leinen, J. R. Ramos-Barrado, R. E. Marotti, E. A. Dalchiele, Thin Solid Films 490 (2005) 124.
[40] M. A. Lucio-López, M. A. Luna-Arias, A. Maldonado, L. M. de la Oliera, D. R. Acosta, Sol. Energy Mater. Sol. Cells 90 (2006) 733.
[41] J. Tauc, R. Grigorovici, A. Vancu, Phys. Status Solidi B 15 (1966) 627.

[42] Annual Energy Outlook 2010 – With Projections to 2035; U.S. Energy Information Administration.
[43] World Water Assessment Programme 2009. The United Nations World Water Development Report 3: Water in a Changing World, UNESCO, Paris; Earthscan London.
[44] H. Goesmann, C. Feldmann, Nanoparticulate Functional Materials, Angew. Chem. Int. Ed. 49 (2010) 1362–1395 (Review).
[45] Y. Zhou, G.R. Patzke, Chimia 64 (2010) 252–258 (Review).
[46] A. Fujishima, K. Honda, Nature 238 (1972) 37–38.

[47] A. Fujishima, X. Zhang, D.A. Tryk, Surf. Sci. Rep. 63 (2008) 515–582 (Review).
[48] D. Zhang, G. Li, J. C. Yu, J. Mater. Chem. 20 (2010) 4529–4536 (Review).
[49] H. Kato, H. Kobayashi, A. Kudo, J. Phys. Chem. B 106 (2002) 12441–12447.
[50] L. Zhang, I. Djerdj, M. Cao, M. Antonietti, M. Niederberger, Adv. Mater. 19 (2007) 2083–2086.
[51] J. Tang, Z. Zou, J. Ye, Angew. Chem. Int. Ed. 43 (2004) 4463–4466.
[52] X.P. Lin, F.Q. Huanga, W.D. Wanga, K.L. Zhang, Appl. Catal. A 307 (2006) 257–262.
[53] L.W. Zhang, Y.J. Wang, H.Y. Cheng, W.Q. Yao, Y.F. Zhu, Adv. Mater. 21 (2009) 1286–1290.
[54] G.Q. Zhang, N. Chang, D.Q. Han, A.Q. Zhou, X.H. Xu, Mater. Lett. 64 (2010) 2135–2137.
[55] L. Zhang, W. Wang, L. Zhou, H. Xu, Small 3 (2007) 1618 – 1625.
[56] G. Xi, J. Ye, Chem. Commun. 46 (2010) 1893–1895.
[57] Y. Zhou, K. Vuille, A. Heel, B. Probst, R. Kontic, G.R. Patzke, Appl. Catal. A 375 (2010) 140–148.
[58] N.C. Castillo, A. Heel, T. Graule, C. Pulgarin, Appl. Catal. B 95 (2010) 335–347.
[59] A. Walsh, Y. Yan, M.N. Huda, M.M. Al-Jassim, S.H. Wei, Chem. Mater. 21 (2009) 547–551.
[60] W. Jeitschko, A.W. Sleight, Acta. Cryst. B 28 (1972) 3174–3178.
[61] W. Jeitschko, A.W. Sleight, Acta. Cryst. B 30 (1974) 2088–2094.
[62] I.S. Cho, C.H. Kwak, D.W. Kim, S. Lee, K.S. Hong, J. Phys. Chem. C 113 (2009) 10647–10653.
[63] H. Dong, Z. Li, Z. Ding, H. Pan, X. Wang, X. Fu, Sens. Actuators B 140 (2009) 623–628.
[64] J. Ungelenk, C. Feldmann, Fotokatalysator, Patent application DE 102010044553.3.
[65] P.S. Yap, T.T. Lim, M. Lim, M. Srinivasan, Catal. Today 151 (2010) 8–13.
[66] T.A. Kandiel, A. Feldhoff, L. Robben, R. Dillert, D.W. Bahnemann, Chem. Mater. 22 (2010) 2050–2060.
[67] R. Lopez, R. Gomez, M.E. Llanos, Catal. Today 148 (2009) 103–108.
[68] Y.K. Leong, B.C. Ong, Powder Technol. 134 (2003) 249–254.
[69] A.F. Hollemann, N. Wiberg, Lehrbuch der Anorganischen Chemie, de Gruyter, Berlin 2007.
[70] B. Wang, G. Ouyang, Y.H. Yang, G.W. Yang, Appl. Phys. Lett. 90 (2007) 121905–121905-3.
[71] S. Gialanella, F. Deflorian, F. Girardi, I. Lonardelli, S. Rossi, J. Alloy. Compd. 474 (2009) 134–139
[72] R. Lacomba-Perales, J. Ruiz-Fuertes, D. Errandonea, D. Martínez-García, A. Segura, Europhys. Lett. 83 (2008) 37002–37002-5.
[73] M.W. Stoltzfus, P.M. Woodward, R. Seshadri, J.H. Klepeis, B. Bursten, Inorg. Chem. 46 (2007) 3839–3850.
[74] K.A. Michalow, D. Logvinovich, A. Weidenkaff, M. Amberg, G. Fortunato, A. Heel, T.J. Graule, M. Rekas, Catal. Today 144 (2009), 7–12.
[75] P. Wang, B. Huang, X. Zhang, X. Qin, Y. Dai, H. Jin, J. Wei, M.H. Whangbo, Chem. Eur. J. 14 (2008) 10543–10546.